

Effects of fault geometry and slip style on near-fault static displacements caused by the 1999 Chi-Chi, Taiwan earthquake

Shiann-Jong Lee^b, Kuo-Fong Ma^a, How-Wei Chen^{a,*}

^a Formerly Institute of Geophysics, National Central University, Taiwan, R.O.C.

^b Institute of Geophysics, Department of Earth Sciences, National Central University, No. 300, Zhongda Rd., Zhongli City, Taoyuan County, 32001, Taiwan, R.O.C

Received 15 June 2004; received in revised form 28 July 2005; accepted 27 September 2005

Available online 21 November 2005

Editor: R.D. van der Hilst

Abstract

We investigated the fault geometry effects and the corresponding coseismic slip distribution using various proposed earthquake fault models for the Chi-Chi earthquake of 21 September 1999. The types of fault geometries are threefold: a simple planar fault plane, a two segmented planar fault plane and a three dimensional (3D) curved fault surface rupture propagation model. We derived the estimated spatial slip distribution from an inversion analysis of GPS coseismic displacement data and show that the 3D fault model is the preferred solution. The simple and segmented fault models lead to significant artificial slip distributions associated with the pre-defined fault geometry and the spatial distribution of GPS stations. The spatial distribution of coseismic slip deduced from the 3D fault model has three observable features: (1) the overall slip is concentrated at depth of less than 12 km, which may well correspond to a shallow-dipping detachment; (2) the maximum slip of about 10 m is located 45 km to the north of the epicenter; and (3) the slip vector is dominated by the dip-slip component. In addition, the results from the inversion of GPS data are consistent with those from the inversion analysis of teleseismic broadband data. A resolution analysis, further, demonstrates that the results are highly correlated with field GPS data studies when we used synthetic test data. The inversion of spatially distributed GPS data is highly sensitive to fault geometry. We conclude that the use of the 3D fault model is not only necessary but also certainly competent enough to well explain the inferred slip style and the observed static coseismic displacements.

© 2005 Elsevier B.V. All rights reserved.

Keywords: Chi-Chi earthquake; fault geometry; inversion; coseismic GPS displacement; slip distribution

1. Introduction

The 21 September 1999 (01:47:12) Chi-Chi earthquake ($M_L=7.3$) was one of the most devastating earthquakes in Taiwan in the past century. Based on thorough geological field surveys of surface breaks, rupture prop-

agation during the earthquake has been interpreted as reverse, left-lateral faulting on a low-angle plane along the Chelungpu fault [1]. The Chi-Chi mainshock is mainly characterized by a long rupture length (over 80 km) with about a 30-s duration time [2]. One distinct feature of the Chelungpu fault is that the surface fault trace turns toward the northeast at its northern tip where the largest final surface displacements are 9.8 m and 5.6 m in the horizontal and vertical directions, respectively. In addition, surface breaks along the Chelungpu fault are complicated in shape and do not continuously follow the

* Corresponding author. Tel.: +886 3 4227151x65203; fax: +886 3 2807062.

E-mail address: hwchen@earth.ncu.edu.tw (H.-W. Chen).

¹ Present address: Institute of Earth Sciences, Academia Sinica, P.O. Box 1-55, Nankang, Taipei, Taiwan, ROC.

original, mapped fault trace. These phenomena are likely indicative of the complexity of the rupture and the non-planar fault geometry of the actual fault system. On account of the limitations of numerical modeling and of the inversion technique for the spatial slip distribution of a finite-fault, previously published studies have been somewhat limited in that they used a planar fault plane or several segments of fault planes based on the complexity of the surface breaks (e.g. [3–6]).

Wang et al. [7] postulated that the thin-skinned thrust model of Suppe [8] would be capable of explaining the tectonic mechanism and fault geometry of the Chi-Chi earthquake. Later, using more than 10^6 small earthquakes to locate and map the active faults of the Chi-Chi earthquake, Carena et al. [9] proposed a 3D fault geometry associated with the main detachment zone which stems from the mountain-building process beneath the Central Range. They asserted that a major seismic basal sliding detachment surface had been formed by the lithological contrast between a weak layer of rock, e.g. shale and limestone, and a zone lacking dense seismicity at about the 10- to 20-km depth. This surface has a slope of about 8° , thus being in agreement with the uplift of the basement high which forms a wedge with over-thrust faulting. The nucleation point of the Chi-Chi earthquake struck at a point where a branch of the fault extends from the decollement but is ramp-bend folded. The rupture surface basically occurred along a weak layer of Chinshui shale that is exposed at surface, thereby creating the Chelungpu fault which conforms with its bedding plane. A deep seismic reflection survey also indicates that the fault dip must have become flatter in the deeper section of the Chelungpu fault [10].

It is not obvious whether the northeast extension of the Chelungpu fault trace originated from the near surface effects caused by the local geology or even if it corresponds to the large asperity on the fault system which itself has not been well-mapped. For a non-planar thrust fault, Oglesby and Archuleta [11] have recently investigated the dynamics of an earthquake rupture on a non-planar fault and have concluded that an abrupt change in dip with depth may, in fact, not be a significant factor in predicting fault slip and low-frequency peak strong ground motion. What has been established in previous studies, however, is that the control of the complexity of slip distribution and ground motion from an earthquake is primarily related to stress distribution and fault geometry near the free surface. Besides this, using the 2D static model, Nielsen and Knopoff [12] showed that changes in strike greatly affect the long-term evolution of a fault system

and may cause different nucleation zones and barriers to rupture.

In this study, without explicitly considering dynamic rupture behavior, we addressed the near surface faulting process by delving into the possible effects of fault geometry on spatial slip distribution, and we did so by inverting densely, well-distributed Global Position System (GPS) data. GPS data have been extensively used to determine the spatial slip distribution over three separated segment faults and to recover the consistent, gross features of seismic data, in line with the work of Johnson et al. [13]. The estimated displacement vectors of Johnson et al. [13], however, do not fit the measurements within an acceptable degree of certainty. The large residuals they obtained may simply be attributed to detail features of the fault geometry. With this in mind, a full investigation of the 3D fault geometry with a systematic analysis of both GPS and seismic data is deemed not only valuable but also necessary. Based on near-fault static GPS data, static slip displacements for surface deformation and slip distribution under the constraints of 3D fault geometry were determined and are discussed in this paper. The results regarding the constraints of fault geometry ascertained here along with the predefined 3D velocity distribution and full waveform 3D Green's function calculation will lay the groundwork to investigate the kinematical rupture process inverted from strong motion data, and those results will be presented in another paper [14].

In our study, to explore the fault geometry effect when using the same inversion scheme to deduce coseismic slip distribution from near-fault static data, we compared the inversion results from three different types of fault geometry: a simple planar fault plane, a two segmented planar fault plane and a 3D curved fault surface rupture propagation model. By virtue of their superior spatial coverage and the fact they also provide a unique opportunity to reconstruct total-slip distributions around the faulting area, we decided to use coseismic GPS records as our data.

2. Data and method

2.1. GPS coseismic displacements

Fig. 1 shows the distribution of the GPS stations and the coseismic displacements during the Chi-Chi earthquake. The data collected from the GPS stations are by far one of the best static data sets ever recorded for the finite analysis of a large earthquake. A total of 131

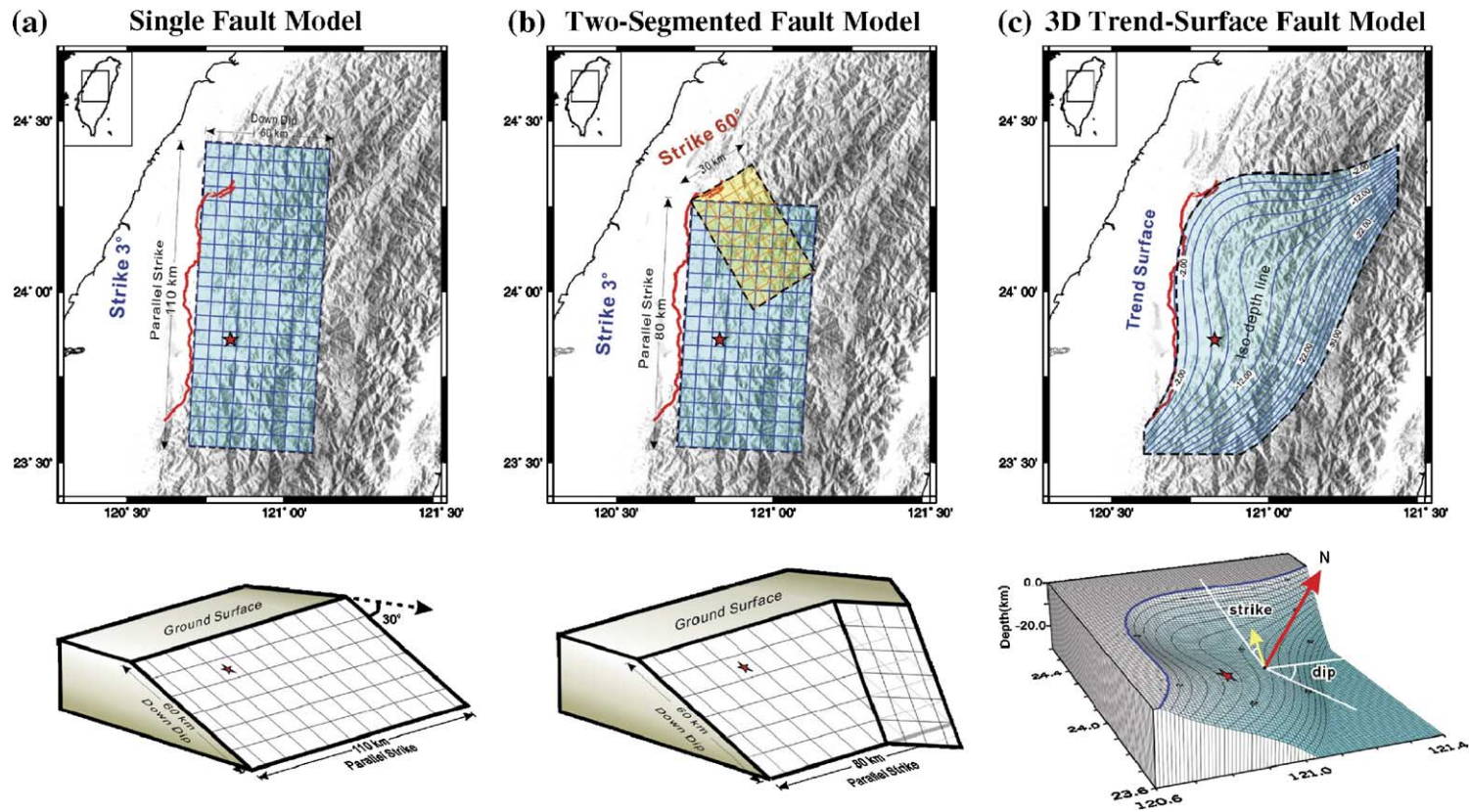


Fig. 2. Three different fault models. The (a) simple planar, (b) two segmented planar bending and (c) 3D fault models used in the inversion. The upper panel displays the map view on the variation of fault geometry showing the surface break (solid line), epicenter (asterisk) and background topography. The lower panel shows the perspective oblique view fault geometry as viewed from the southern border. The thin solid lines indicate the iso-depth lines of the fault plane.

geodetic data for other large earthquakes, including the 1983 Imperial Valley earthquake [17], the 1992 Landers earthquake [18] and the 1994 Northridge earthquake [19].

2.3. Construction of fault models

Fig. 2 shows the three different types of fault geometry both in map form (upper panel) and from an oblique view (lower panel). From the surface breaks, the Chelungpu fault exhibits an average strike of about N3°E and a dip of about 29° to the east [1]. The freshly exposed fault traces bend toward the northeast at its northern tip about 45 km away from the epicenter. To determine the effect of fault geometry inverted from the same near-fault static displacement data set, we first attempted to model the Chi-Chi earthquake with a single fault plane (Fig. 2a). This model with a simple planar fault plane geometry has a strike of 3° and dip of 29° to the east, which is consistent with the general trend of surface breaks. To incorporate the bending tip of the fault trace, we adopted a two segmented faulting model, as shown in Fig. 2b. While maintaining the same dip angle of 29°, the two segmented planar fault yields a different strike direction of N3°E and N60°E. The intersection between the two planar faults is shown in the lower panel of Fig. 2b.

The actual fault systems of the Chi-Chi earthquake have highly heterogeneous slip distributions and very complicated shapes, just like that which is often observed in field surveys of surface breaks. For a complex fault geometry, however, the strike and dip typically varies at different positions along the fault, perhaps therefore making optimized 3D surface to the earthquake locations necessary. In accordance with Carena et al. [9] and to avoid the overlapping area created by the second model, we constructed the optimum 3D fault geometry by performing a trend surface analysis via cubic spline interpolation. The estimated fault geometry was based on the available data from the ruptured fault exposed on the surface and 327 well relocated after-

shocks (Fig. 2c). The relocated hypocenters are determined by using the method of Joint Hypocenter Determination (JHD). We inferred the attitude of the fault plane from the relocated seismicity clustered from the focal mechanisms of both mainshock and aftershocks, geology, dip angle derived from direct measurements of permanent slip along fault trace and near-fault drilling data. Two features predominate in our proposed trend surface model. For one, the best-fitted smoothed surface preserves the main features in the northern portion of the fault plane. Additionally, the dip angle in the deeper portion (~10–15 km) of the fault is nearly horizontal (about 7–8°) but quickly bends upward as the fault rupture reaches the surface, which corresponds to the thin-skinned thrust model from the seismic reflection experiment described by Wang et al. [10,20]. Just as initially expected, the refined 3D fault geometry from our near-fault GPS data provides a much better solution. By contrast, for the single and two segmented planar fault plane model, each subfault patch has a length and down-dip width of about 10 km in the finite-model modeling. To accommodate 3D fault geometry, we mapped each subfault onto the trend surface, and we were able to slightly overlap the plane domain of each individual subfault or slightly separate them from each other. The total subfault number for the 3D fault surface geometry is 49. The parameters of each of the three fault models used in this study are listed in Table 1.

2.4. Inversion results

To examine the effect from different fault geometries by comparing the estimated source faulting slip-pages extracted from GPS observations, first of all we calculated the spatial slip distribution from the single planar fault plane geometry. Fig. 3a and b present the results of the comparison between the synthetic and observed GPS horizontal and vertical displacements at each GPS station. The horizontal components correspond well both in slip amplitude and direction for

Table 1
Parameters used in the three types of fault geometry

Model	Simple planar fault	Two segmented planar fault	3D smoothed trend surface fault
Data number		131 _{stations} × 3 _{components}	
Subfault number	66 (10 × 10 km ²)	48, 18 (10 × 10 km ²)	49 (10 × 10 km ²)
Subfault mechanisms			
Strike	30°	30° and 60°	Follow the trend surface
Dip	30°	30°	
Rake	Free from 0–90°	Free from 0–90°	

The inversion was performed using the same near-fault GPS static displacement data.

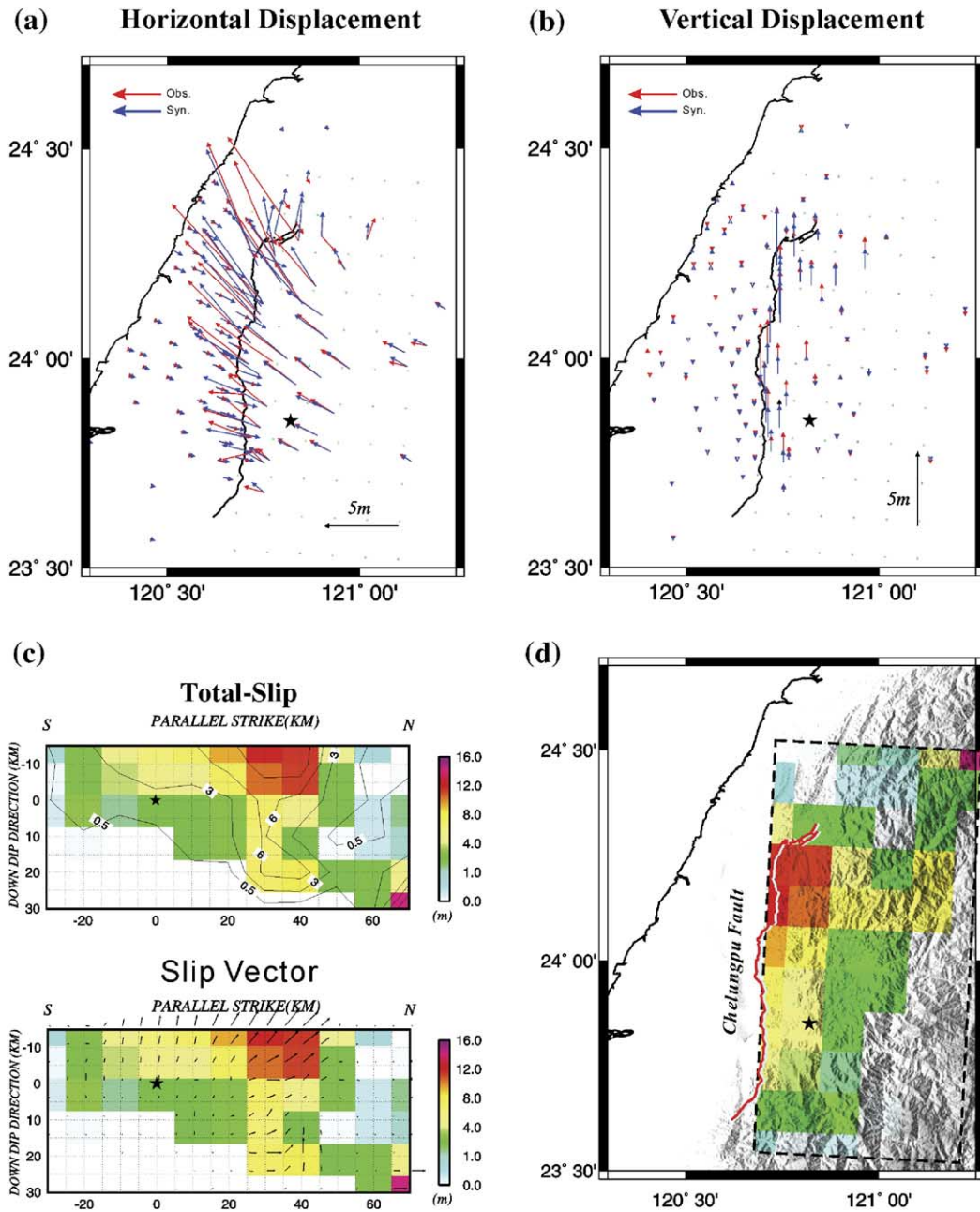


Fig. 3. Comparisons of the synthetics (blue arrows) and observations (red arrows) for the (a) horizontal and (b) vertical coseismic displacements from GPS data for the single fault model. The red solid lines indicate the surface break of the Chelungpu fault, and the asterisk (in black) indicates the epicenter. (c) Total-slip distribution and slip vectors over the single fault plane. The degree of slip is indicated by shading and contouring, as shown in the legend. The arrows indicate the slip direction on the rupture plane. (d) Map view of total-slip distribution and the background topography.

most stations except for those located in the northern part of the fault. Inconsistencies in the vertical component, on the other hand, are somewhat pronounced, especially on the hanging wall of the fault. Fig. 3c and d show that at depth range between the surface and the location of the mainshock most of the slip vectors

are mainly oriented in the up-dip direction. However, the inferred slip vectors below the nucleation point of the mainshock, i.e., between the depths ranges of 0–25 km, are dominated by the strike-slip motion. The largest slip, about 12 m, is located at the corner where the fault turns toward the northeast even though the bend-

ing effect was not specifically taken into account in the proposed simple fault geometry model. Apart from this, an unambiguous large slip area is located in the northernmost bottom portion (within the depth range of 20–30 km) of the fault plane. Because the spacing of

GPS stations is sparse in that area, the inversion procedure had to be less constrained when it came to resolving the inverted slip distribution in that particular fault region. The synthetic horizontal slip vector shows obvious inaccuracies near the bending of the Che-

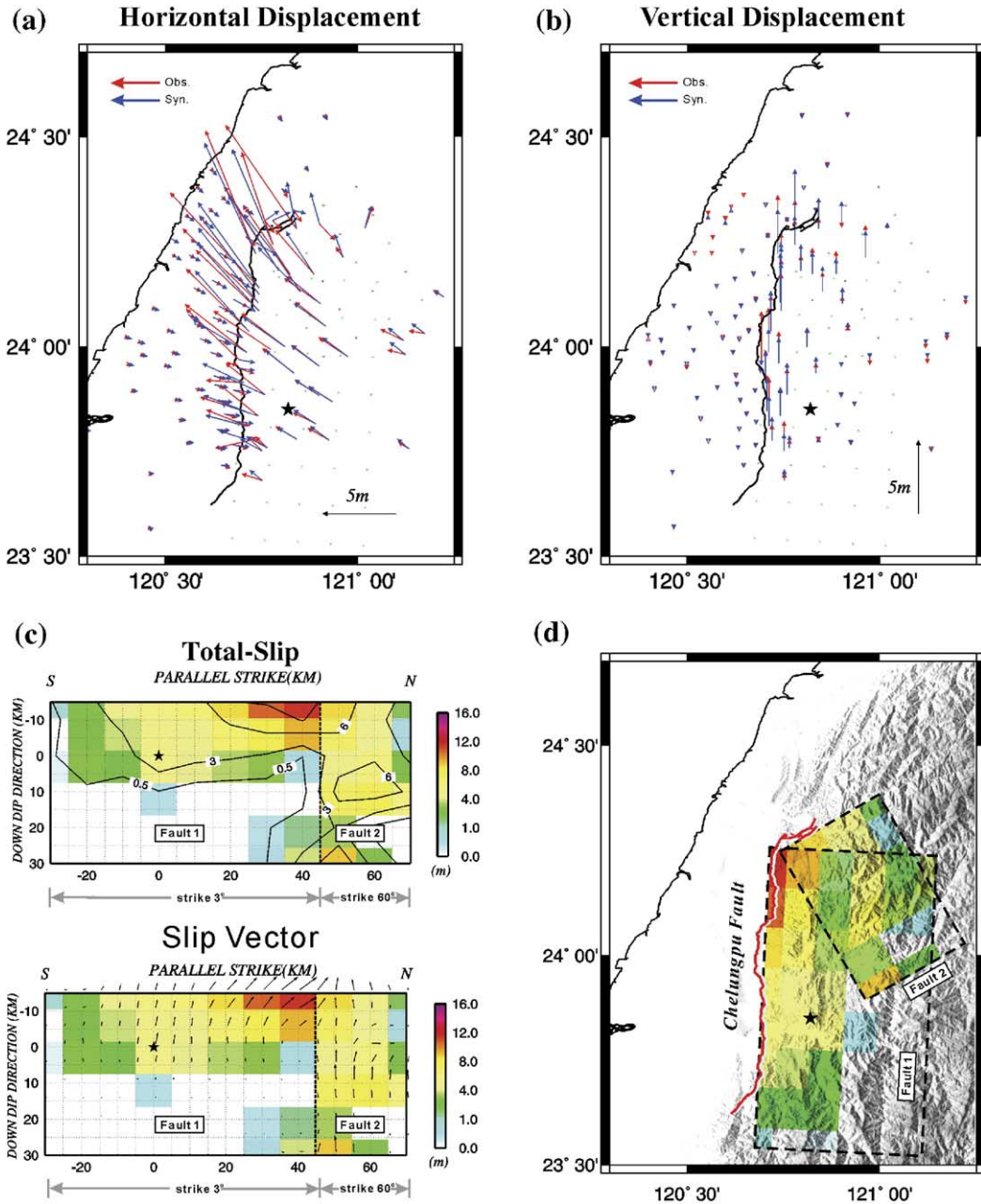


Fig. 4. Comparisons of the synthetics (blue arrows) and observations (red arrows) for the (a) horizontal and (b) vertical coseismic displacements from GPS data for the two segmented fault plane model. The red solid lines indicate the surface breaks of the Chelungpu fault, and the asterisk (in black) indicates the epicenter. (c) Total-slip distribution and slip vectors over the bending fault plane. The amount of slip is indicated by shading and contouring, as shown in the legend. The arrows indicate the slip direction on the rupture plane. (d) Map view of the total-slip distribution accompanying the background topography.

lungpu fault. The misfit (σ) in the first proposed model is 0.219.

The two segmented fault plane geometry takes on the main features of the bended fault plane, but not completely. Because two fault planes (faults 1 and 2) intersect, it was initially expected that the estimated

slips in the overlapped region would be able to be resolved automatically by the inversion solver. Using such parameterization of fault geometry, the inverted slip distribution is allowed on both segments even in the region where they overlap. Fig. 4a and b show the estimated displacement vector at each surface GPS

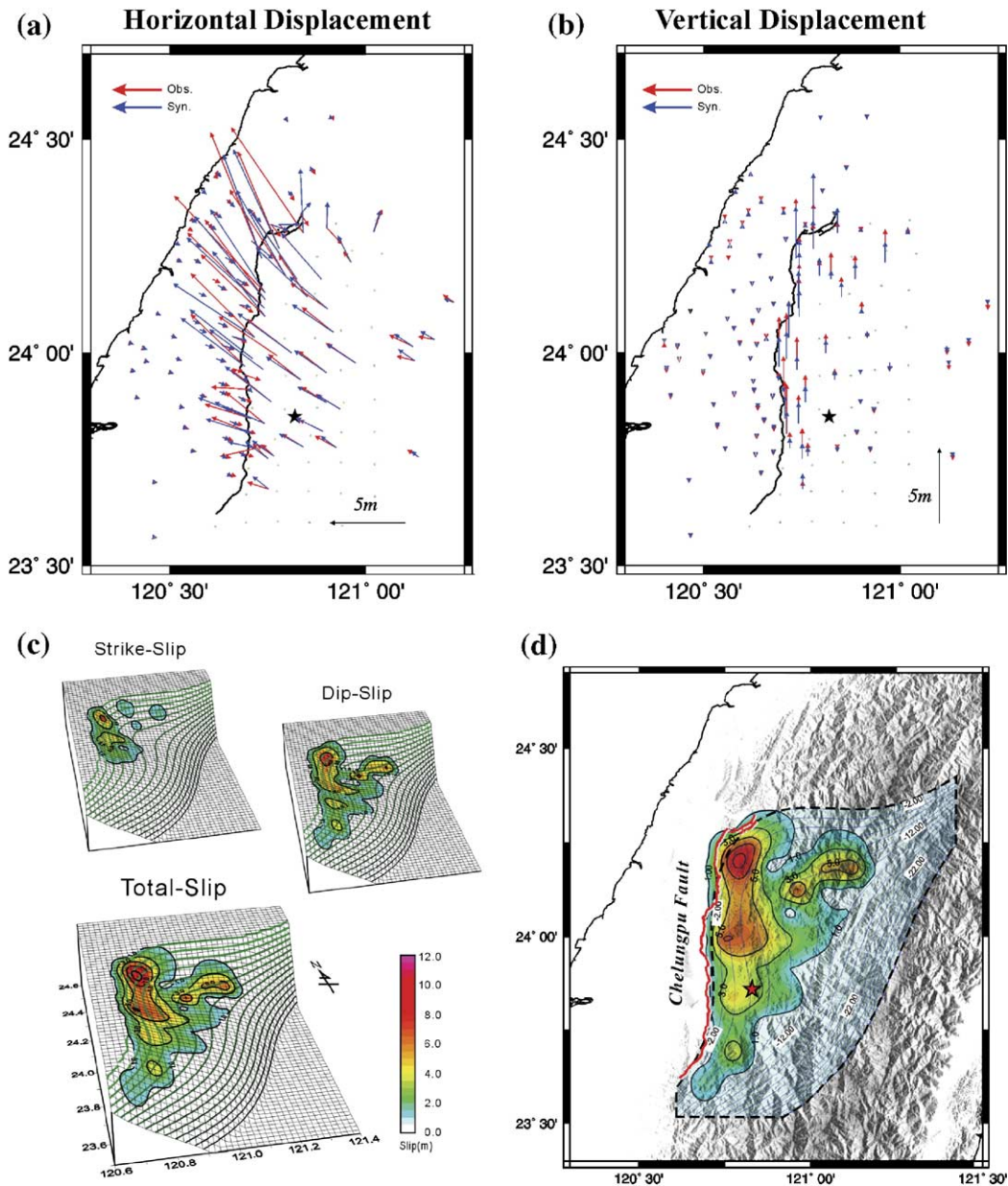


Fig. 5. Comparisons of the synthetics (blue arrows) and observations (red arrows) for the (a) horizontal and (b) vertical coseismic displacements from GPS data for the 3D fault model. The red solid lines indicate the surface break of the Chelungpu fault, and the asterisk (in red) indicates the epicenter. (c) Perspective oblique view of the strike-slip, dip-slip and total-slip distribution over the 3D fault plane. The amount of slip is indicated by shading and contouring, as shown in the legend. (d) Map view of total-slip distribution with the background topography. The solid lines indicate the iso-depth lines on the fault plane.

station. Compared to the single planar fault plane geometry, the inversion results from the proposed second model is more efficient in explaining most of the observations, particularly those for stations in the northern portion of the fault. Fig. 4c and d show the inverted spatial slip distribution from this model. The slip amplitude and direction in the shallow part of fault 1 are similar to the results derived from the simple planar fault model. Most of the slips at the shallow part are mainly along the down-dip direction (Fig. 3). By contrast, in fault 2, slip vectors with a magnitude of 6 to 10 m are distributed almost over the entire fault plane. These inversion results may imply that rupturing is predominant in the deeper portions of fault 2. Since the slips in the deeper portions are located where these two faults overlap, the contribution from each individual fault segment cannot be clearly resolved owing to the trade-off involved in the inversion scheme. In sum, it is justified to state that artifacts associated with the two segmented fault geometry produce unclear slips in the deeper portions where the two planes overlap. The misfit of this model is 0.164.

Turning to the proposed 3D fault geometry, the inversion results are given in Fig. 5c and d together with the 3D trend surface fault model. On account of the difficulty involved in data visualization, unlike those in Fig. 3 and 4 derived from the two previous models, the slip distributions are represented on a color scale and with contouring rather than with vectors and patches along the fault plane. The inversion results indicate that most of the slips occur at depths of less than 12 km. Notably large slips with a magnitude over 3 m are concentrated at the depth range of 4–8 km and coincide with the ramp of the detachment. Strike-slip components are predominant in the central and northern portions of the faulting. The largest slip is near the bending of the fault about 45 km north of the epicenter. Another prominent large asperity is located east of the largest slip region where rupturing occurred at the depth of about 12 km with a slip amplitude of more than 5 m. Although a fairly large rupture surface is shown, the estimated slip remains well constrained in the shallow portion of the fault surface, with the overall slip located above the 12 km iso-depth contour. Comparing the horizontal and vertical static displacements shown in Fig. 5a and b, both the observed and synthetic displacements are well correlated with each other except for a few for GPS stations where the smoothed trend surface does not coincide with the actual fault trace. For the representative 3D fault geometry, the synthetic surface displacements satisfactorily explain the observations

(Fig. 5b). The misfit is 0.116, the smallest value among the three models.

3. Discussion

3.1. Model resolution test

To examine the effects of fault geometry on the resolution of spatial slip distribution, we conducted a resolution analysis by generating two sets of slip distributions which we inverted for two different predefined fault geometries, namely a 3D curved surface and a simple planar fault plane model. Given the trade-off we observe in the previous inversion study of our field data, we did not consider the two segmented planar fault model in our investigation. Our two sets of synthetic test models consist of a simplified dislocation patch, one located in the middle portion (Fig. 6) and the other at the northern bending tip (Fig. 7). Both synthetic test models have a 10-m pure dip-slip component at a depth ranging between 0 and 5 km. We then compared the imaged dislocations to identify the characteristics of the geometric effects and the trade-offs involved in the inversion scheme.

Fig. 6 compares the slip distributions of the true model with those obtained from the predefined full 3D fault surface and the single planar fault geometries. The true solutions in Fig. 6a are pure dip-slip patches located in the middle portion. For the inverted results using full 3D fault geometry (Fig. 6b), the peak slip in the imaged rupture distribution is only 8.7 m (i.e., 1.3 m less), and the inverted total-slip area is slightly larger than that of the actual dislocation size. True that some extra slip vectors with amplitude of less than 2 m appear in the dip-slip components at depths of ~10 km, but of importance is that the major imaged slip patch is primarily consistent with the correct one. Also, in the 3D fault geometry, some small slip amplitudes of less than 0.5 m appear in both the strike-slip and dip-slip components at depths beyond 22 km, but this has no significant influence on overall slip distribution. For the most part, it can be said that the resolution of the inverted slip distribution in the middle region of the fault based on the 3D fault model is reliable.

Fig. 6c shows the imaged slip distribution over a single plane fault model. The inverted slip is evidently much shallower than that in the true model, and the estimated peak slip amplitude is greater than 10 m. In addition, a significant number of pseudo-slip patches are distributed in the bottom portion near the northern corner of the fault which is dominated by the strike-slip component. The finding of such inversion artifacts

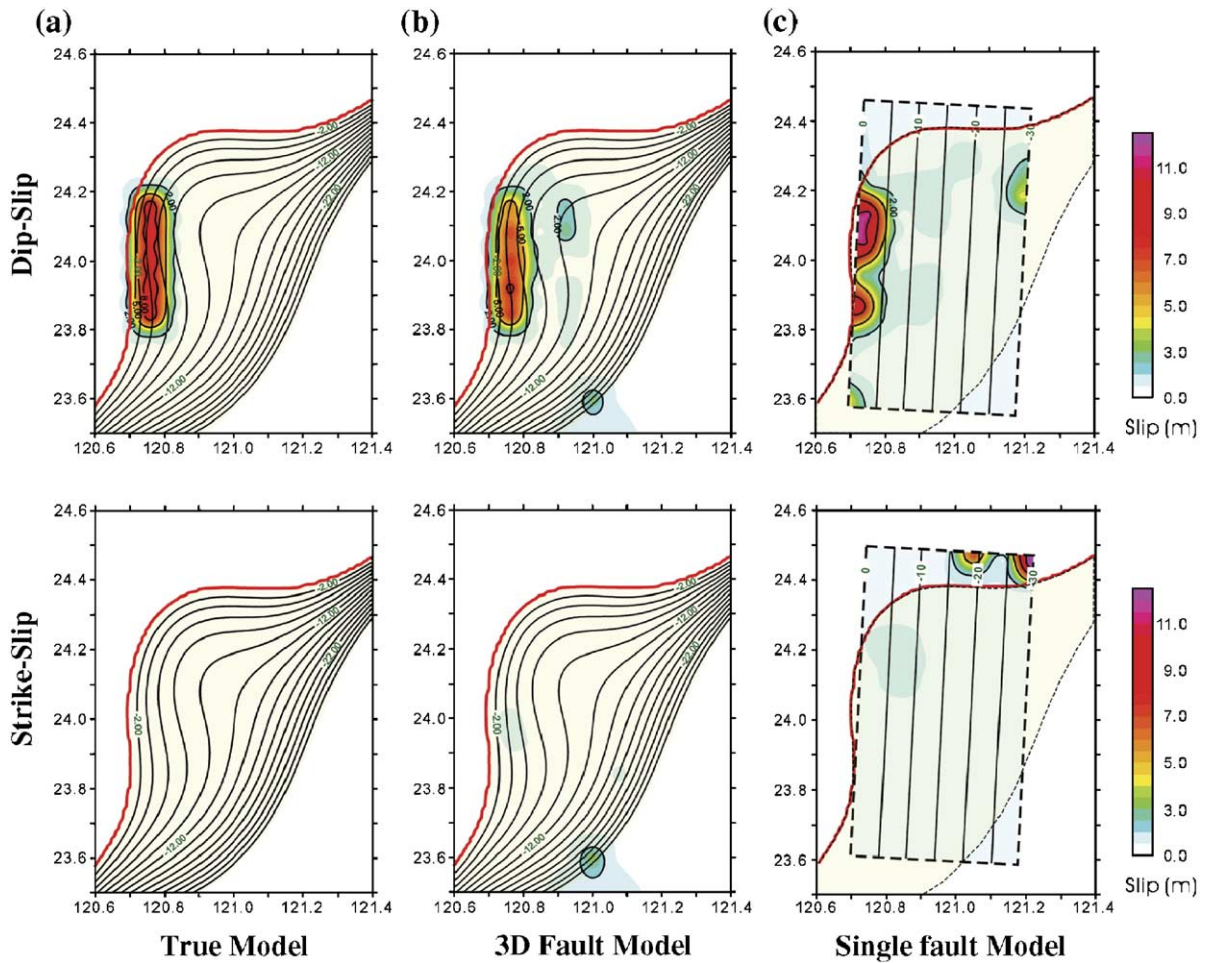


Fig. 6. Resolution analysis under the assumption of pure dip-slip faulting with maximum slip amplitude of 10 m within the depth range of 0 to 5 km located in the middle segment of the Chelungpu fault. The inversion results of the synthetic test model for the (a) true solution, (b) 3D fault model and (c) single fault model. Both dip-slip (upper panels) and strike-slip (lower panels) components are displayed for detailed comparison. The inverted slip distribution for the single fault model is not acceptable.

generated by the simple planar fault geometry is consistent with phenomena which arise from real data applications, as shown in Fig. 3c and d.

Subsequently, we used a similar approach here to test the effect of fault geometry where a large pure dip-slip patch is located at the bending tip (Fig. 7a). The inverted slip image on the 3D fault model has a broader dislocation size than that in the known solution (Fig. 7b) and is accompanied by a strike-slip component of less than 1 m (artifact). The main location of the slip patch is again clearly consistent with the actual solution. However, the peak slip amplitude, with a value of 7.4 m (i.e., 2.6 m less), is underestimated and creates a fairly blurred image when compared with that of the true model. Some inverted dip-slip components exist in deeper portions (~16 km) and have an amplitude value of less than 1 m.

As for the single planar fault model (Fig. 7), the inverted image is by far worse, and the findings, in fact, provide solid evidence that inversion with simple plane fault geometry is not suitable for Chi-Chi earthquake data. To explain this, the main location of the slip region shifts farther to the east and deepens with a peak slip amplitude larger than 10 m. Furthermore, in the imaged dip-slip component, subfault patches—rather small both in size and amplitude—are scattered around the mislocated main dislocation. A notable extra slip patch is also created by the inversion technique within the depth range of around ~25 km. Aside from this, some strike-slip components rupturing at the southern end of the fault are not reasonable. Thus, it can be concluded with confidence that when trying to reconstruct the precise slip distribution at a bending tip, the use of single planar fault plane geometry to

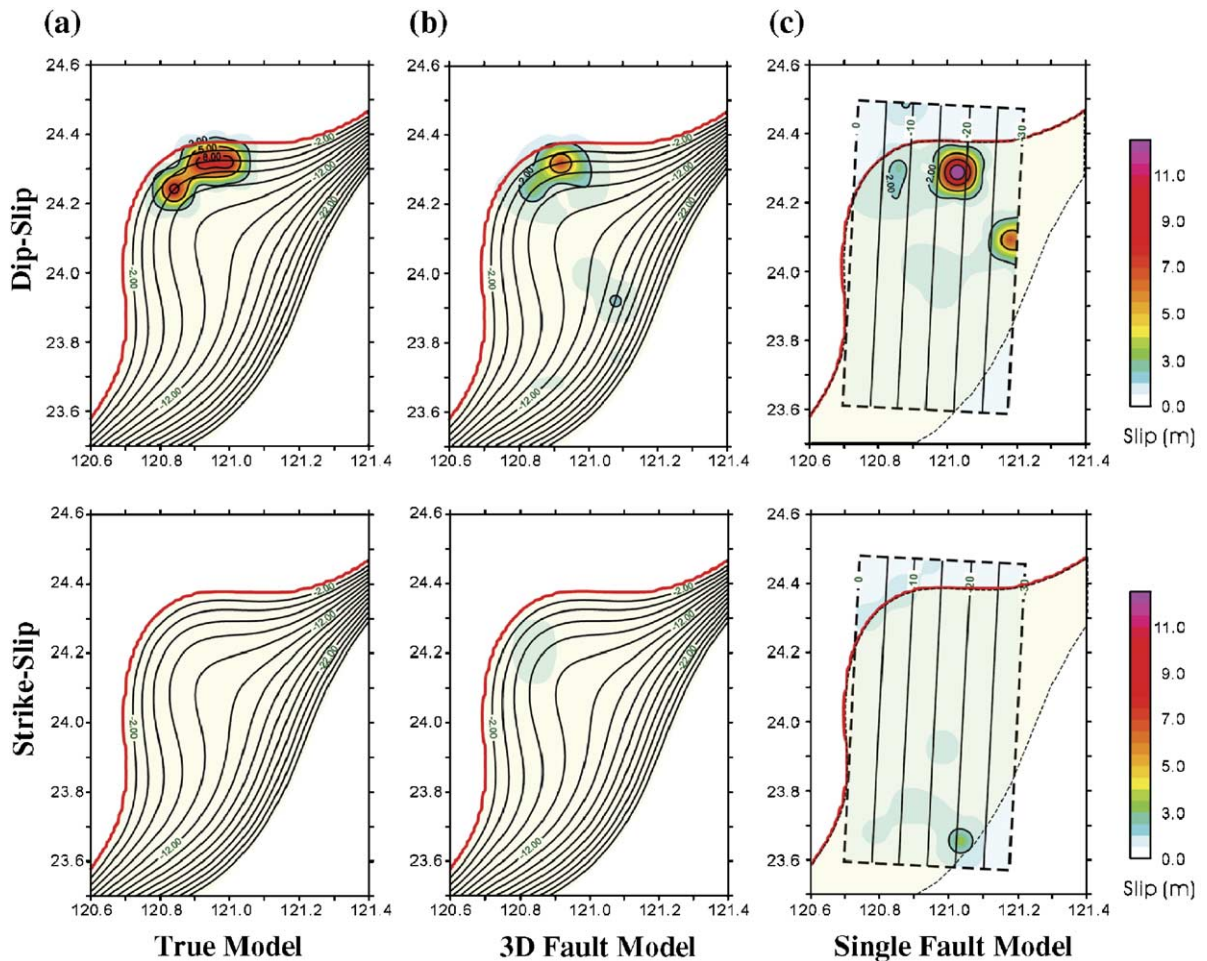


Fig. 7. Resolution analysis. In contrast to the test model shown in Fig. 6, the pure dip-slip rupture patch is located at the northern bending tip with maximum slip amplitude of 10 m ranging from 0 to 5 km in depth. The inversion results of the synthetic test model are given for the (a) true solution, (b) 3D fault model and (c) single fault model. Both dip-slip (upper panels) and strike-slip (lower panels) components are displayed for detailed comparison. Compared with the results shown in Fig. 6, it is most evident that fault geometry considerably affects the inversion results.

image a complex fault system is difficult, to say the least.

Comparing the inverted total-slip distributions, as shown in Figs. 6 and 7, it is apparent that an accurate description of fault geometry, especially where the orientation of the surface fault break turns, may considerably affect the inversion results. In addition, the synthetic tests suggest that when surface measurements are used, the estimated slip vector in the northern deeper portion is less reliable on account of inaccuracies in the description of the fault geometry. Furthermore, from our resolution analyses, we believe that planar fault geometry overestimates the rupture property, while the more reasonable 3D fault geometry tends to underestimate the slip amplitude and the inverted rupture area. Bearing these findings in mind, we reach the conclusion that, most assured-

ly, an accurate description of fault geometry is necessary and even crucial when attempting to obtain reliable results with regard to the amplitude and direction of slips.

3.2. Comparison with surface breaks

Fig. 8 compares the horizontal (Fig. 8a) and vertical (Fig. 8b) static displacements, as predicted by 3D fault geometry and GPS observations. The misfit between the observed and inferred horizontal displacement components is an acceptable 0.038. Some discrepancies showing differences of more than 1 m can perhaps be attributed to local variations in fault orientation which cannot be fully explained by the best estimated trend-surface fault geometry. On the other hand, the inaccuracy in the vertical component

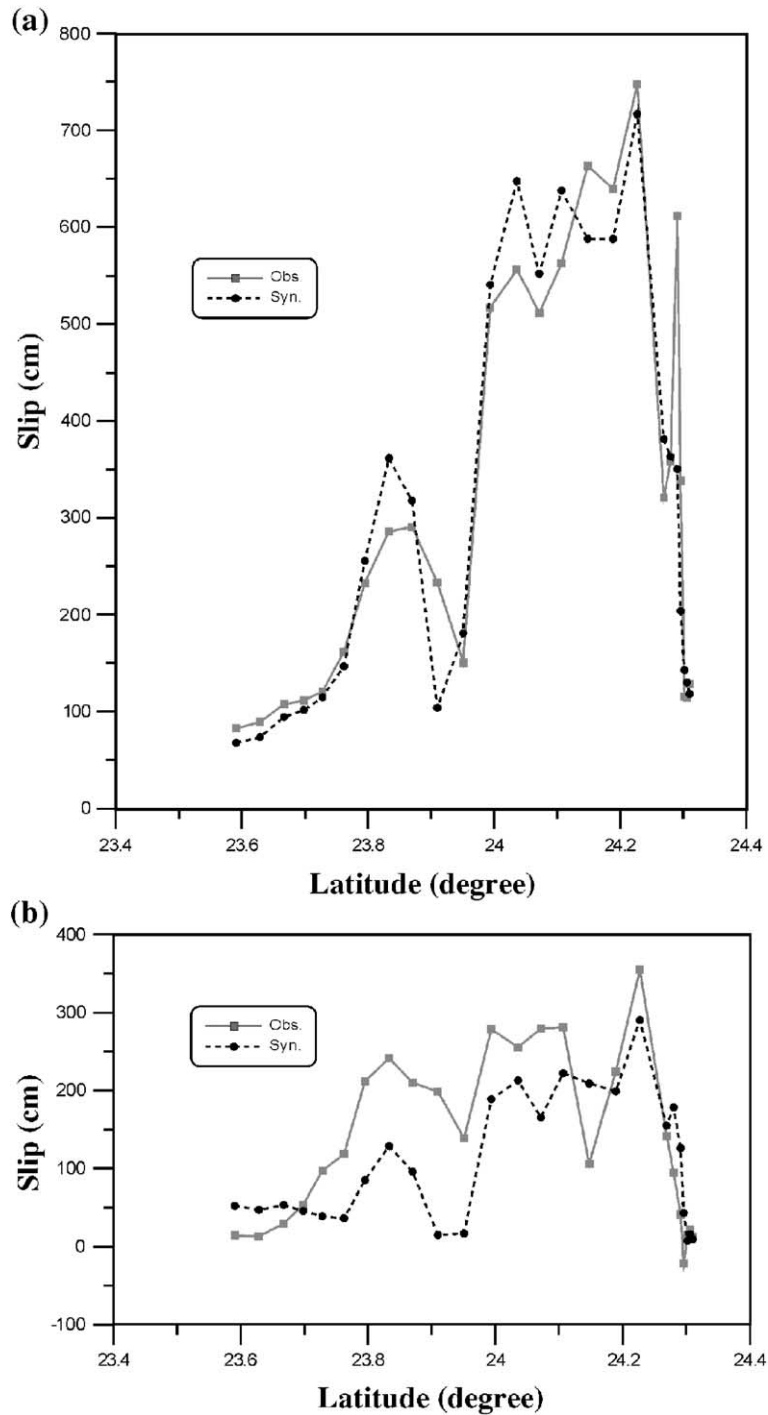


Fig. 8. Comparisons of surface-slip predicted by 3D fault geometry and GPS observations. (a) and (b), respectively, present the horizontal and vertical components of static displacement along the fault trace. The solid lines with square symbols represent the observations. The dotted lines with black dots represent the synthetics. The positions along the surface fault trace are indicated by latitude in degrees.

displacement with a misfit of 0.217 is larger than that in the horizontal component displacement. Despite this, inaccuracies inherent in the measurements and

processing of GPS data should be taken into account. Such discrepancies might have mainly been caused by variations in rigidity across the fault, which we did not

take into consideration in our Green's function calculations. Alternatively, they could have been a result of variations in the effects from local geology and topography. Still another possibility is that the half-space model of Green's function calculations produced less well constrained GPS coseismic displacements for the vertical component.

3.3. Comparison with results from the inversion of teleseismic data

Fig. 9 compares the final slip distribution derived from the 3D fault model based on near-fault static displacements with the results from the inversion of teleseismic data [3,22]. Though both the fault geometry and data sets are different, the main features of the total-slip distribution patterns are similar. Most of the slip is concentrated in the shallow part of the fault surface (about 0 to 10 km), with the largest slip being near the bending tip. Two different types of data sets were used here for the Chi-Chi earthquake, but a notably large asperity is located in the deeper part near longitude 121.1 and latitude 24.2. Somewhat surprising here perhaps might be that the total seismic moment release with teleseismic inversion is about 60% less than that

from GPS inversion. However, it should be kept in mind that this difference may have resulted from the different frequency band used in the two data sets. That notwithstanding, in addition to the well correlated total-slip distribution shown in Fig. 9, the location of the aftershock sequence (from 21 September 2000 to November 2000) provides solid evidence that the solution using the Chi-Chi mainshock data can be well resolved. Such a finding is even better constrained by using near-fault GPS data with the inclusion of 3D fault geometry. Our comparison also indicates that the inversion of teleseismic data is less influenced by fault geometry and that the amount of slip over the fault plane is less well resolved.

Table 2 lists the estimated source parameters for the three different types of fault geometry discussed in this paper. The seismic moments derived from the inversion of GPS data for a simple fault plane, a two segmented planar fault plane and a 3D curved fault surface geometry model are 1.68, 1.76 and 1.30 ($\times 10^{27}$ dyne cm), respectively. Worth noting is that the seismic moment determined from our 3D fault model is different from the Harvard CMT solution (4.1×10^{27} dyne cm). What may have led to this difference are the point source approximation as well as the body waves

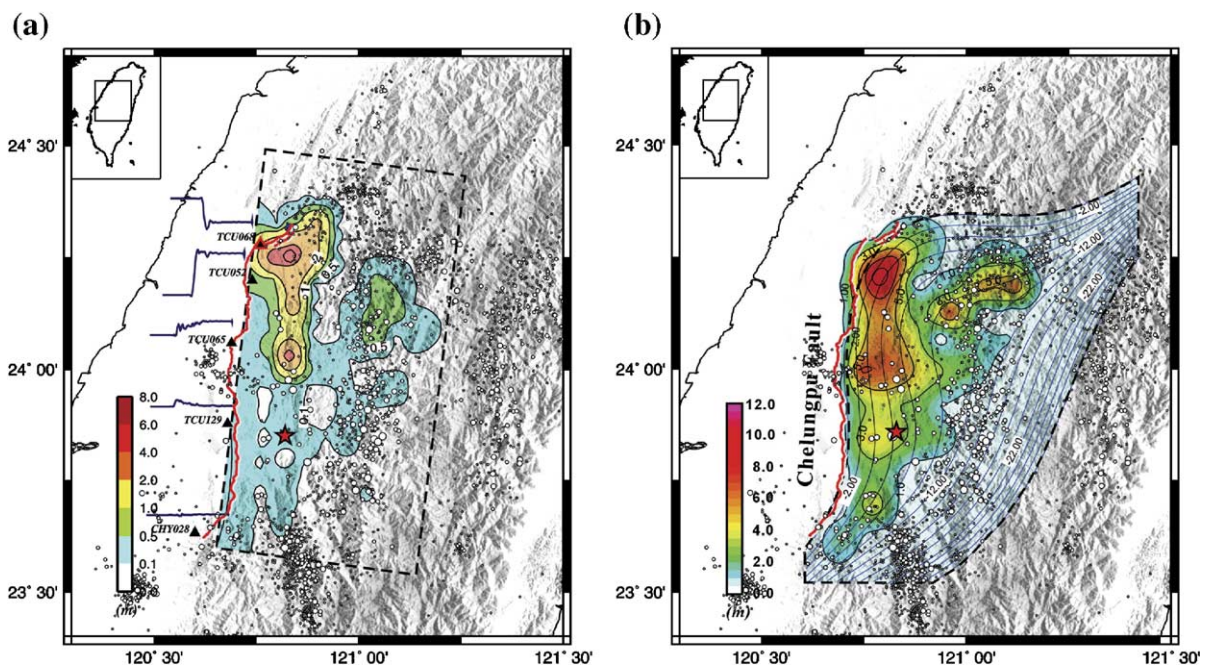


Fig. 9. Comparisons of slip distributions inverted from (a) teleseismic data with simple planar fault geometry and (b) GPS data with 3D fault geometry. The rough solid line (in red) indicates the surface break of the Chelungpu fault. The asterisk indicates the epicenter. The open circles indicate the aftershocks which occurred between 20 September 2000 and November 2000 with various magnitudes ranging from M_L 6 to M_L 1, as recorded by the CWB. The fine solid lines (in blue) are the iso-depth contours over the pre-defined 3D smoothed trend surface fault plane. The degrees of slip are indicated by shading and contouring (in rainbow), as shown in the legend.

Table 2
Estimated source parameters inferred from the three different fault models

Model	Mechanism: strike, dip, rake			Moment (*10 ²⁷ dyne cm)	Average slip ^a (m)	Stress drop (bar)	M_w
Simple planar fault	3	30	Free ^b	1.68	5.86	15.6	7.55
Two segmented planar fault	3/60	30/30	Free ^b /Free ^b	1.76	5.90	16.4	7.56
3D trend surface fault	All free in the reasonable range			1.30	2.61	12.1	7.48

^a Average slip amplitude calculated from all subfaults.

^b Free from 0° to 90°.

used in the CMT inversion analysis. Different types of data and frequency content may have also contributed to the difference. The average slip within the faulting region is estimated to be in the range of 2.6 to 5.9 m. Under the assumption that there is a rectangular fault rupture model on each 10 km × 10 km subfault, the stress drop [22] for each of the three fault models is 15.6, 16.4 and 12.1 bar, respectively. The moment magnitude (M_w) is about 7.5, which also agrees with the $M_w=7.2$ magnitude estimated from teleseismic moment tensor inversion.

4. Conclusions

Our investigation into the effects of fault geometry and slip style on the inversion of near-fault GPS data from the 1999 Chi-Chi, Taiwan earthquake demonstrates that selecting the most appropriate model is central to the task. Significant differences among the models may result in misallocated slip distributions and an erroneous interpretation of rupture history and wave propagation phenomena. Compared with the artificial slips associated with the pre-defined simple-plane fault and two segmented planar fault geometries, the results clearly point to 3D fault geometry as the best model by far. The resolution tests also confirm our conclusion.

The slip distribution derived from the smoothed 3D trend surface fault model shows that most of the slip is concentrated over the shallow part (with two main rupture areas at depth range between 4–8 and 10–12 km) of the fault dominated by the dip-slip components. The proposed 3D fault model also distinctly points out that the deepest part of the slip area is just above the decollement described in the thin-skinned model. The maximum slip of about 10 m is located 45 km north of the determined epicenter. Such a large asperity is located right near the bending tip of the surface break that cuts across the abutment of the Shigan dam, giving rise to a 9.8 m vertical displacement in the body of the dam. The effect on non-planar fault geometry, particularly the abrupt change in dip along the depth direction,

is strongly correlated with both the distribution of aftershock clusters and the inversion results of low amplitude slip distribution inferred from field data (Fig. 5) and synthetic test studies (Fig. 6). The geometry of the bending tip to the north of the Chelungpu fault also affects the final inversion results due to the azimuth coverage of the GPS stations and inversion of the near-fault static vector displacement data shown in the field (Fig. 5) and synthetic cases (Fig. 7). In our study, the inversion of the densely distributed near-source GPS data is very sensitive to fault geometry; therefore, using the 3D fault model is necessary, and on the capability side, it (appears to be) is highly efficient as far as explaining observed near field GPS data goes. The actual fault systems, nevertheless, have highly heterogeneous slip distributions and are very complicated in terms of shape, as is frequently observed from field surveys of surface breaks. The misfit may also be attributed to the heterogeneity of the media and topography as well as to inelastic deformation, all of which were ignored in our current model. Hence, using the smoothed 3D trend surface to approximate the actual fault system may still under-estimate the natural behavior of the rupture process. This finding is also reflected in our resolution analysis and in the comparison of the source parameters derived from different fault geometries. Nevertheless, we conclude with confidence that the use of the 3D fault model is not only necessary but also certainly highly competent in explaining the inferred slip style and the observed static coseismic displacements.

Acknowledgments

The authors would like to dedicate this work to people who suffered most during this catastrophe period caused by the devastating Chi-Chi earthquake in Taiwan. We wish to thank Dr. S. B. Yu for providing GPS data. Some of the figures were generated from GMT software by P. Wessel and W. H. F. Smith. We thank two reviewers, Drs. D. D. Oglesby and S. B. Yu, for their helpful suggestions to improve this manuscript

to be timely published. Thanks should be extended to editor, Robert Van der Hilst, in making most figure presentations legible. This study was partially supported by the National Science Council, R.O.C., under Grant NSC 89-2921-M-008-012-EAF (K.F. Ma and S. J. Lee). H. W. Chen gratefully acknowledges the continuous funding supports from National Science Council, R.O.C., under Grant Numbers NSC 89-2921-M-194-006-EAF, and NSC 90-2119-M-194-006.

References

- [1] C.T. Lee, K.H. Kang, C.T. Cheng, C.W. Liao, Surface rupture and ground deformation associated with the Chi-Chi, Taiwan earthquake, *Sino-Geotech.* 81 (2000) 5–18.
- [2] K.F. Ma, C.T. Lee, Y.B. Tsai, T.C. Shin, J. Mori, The 1999 Chi-Chi, Taiwan ($M_L=7.3$, $M_w=7.7$) earthquake—large surface displacement on an inland thrust-fault, *EOS* 80 (1999) 605–611.
- [3] K.F. Ma, T.-R. Song, S.J. Lee, S.I. Wu, Spatial slip distribution of the September 20, 1999, Chi-Chi, Taiwan, earthquake—invited from teleseismic data, *Geophys. Res. Lett.* 27 (2000) 3417–3420.
- [4] K.F. Ma, J. Mori, S.J. Lee, S.B. Yu, Spatial and temporal distribution of slip for the 1999 Chi-Chi, Taiwan earthquake, *Bull. Seismol. Soc. Am.* 91 (2001) 1–19.
- [5] C.J. Wu, M. Takeo, S. Ide, Source process of the Chi-Chi earthquake: a joint inversion of strong motion data and Global positioning system data with a multifault model, *Bull. Seismol. Soc. Am.* 91 (2001) 1128–1143.
- [6] W.C. Chi, D. Dreger, A. Kaverina, Finite-source modeling of the 1999 Taiwan (Chi-Chi) earthquake derived from a dense strong-motion network, *Bull. Seismol. Soc. Am.* 91 (2001) 1144–1157.
- [7] Chen Ji, D.V. Helmberger, T.R.A. Song, K.-F. Ma, D.J. Wald, Slip distribution and tectonic implication of the 1999 Chi-Chi, Taiwan, earthquake, *Geophys. Res. Lett.* 28 (2001) 4379–4383.
- [8] C.Y. Wang, C.H. Chang, H.Y. Yen, An interpretation of the 1999 Chi-Chi earthquake in Taiwan based on the thin-skinned thrust model, *TAO* 11 (2000) 609–630.
- [9] J. Suppe, Mechanics of mountain-building and metamorphism in Taiwan, *Mem. Geol. Soc. China* 17 (1981) 1–16.
- [10] S. Carena, J. Suppe, H. Kao, The active detachment of Taiwan illuminated by small earthquakes and its control of first-order topography, *Geology* 30 (10) (2002) 935–938.
- [11] C.Y. Wang, The detection of a recent earthquake fault by the shallow reflection seismic method, *Geophysics* 67 (2002) 1345–1352.
- [12] D.D. Oglesby, R.J. Archuleta, The three-dimensional dynamics of a non-planar thrust fault, *Bull. Seismol. Soc. Am.* 93 (2003) 2222–2235.
- [13] S.B. Nielsen, L. Knopoff, The equivalent strength of geometrical barriers to earthquakes, *J. Geophys. Res.* 103 (1998) 9953–9965.
- [14] S. Johnson, Y.J. Hsu, P. Segall, S.B. Yu, Fault geometry and slip distribution of the 1999 Chi-Chi, Taiwan earthquake imaged from inversion of GPS data, *Geophys. Res. Lett.* 28 (2001) 2285–2288.
- [15] S.J. Lee, K.F. Ma, H.W. Chen, Three dimensional dense strong motion waveform inversion for the rupture process of the 1999 Chi-Chi, Taiwan, Earthquake, *J. Geophys. Res.* (submitted for publication).
- [16] S.B. Yu, L.C. Kuo, Y.R. Hsu, H.H. Su, C.C. Liu, C.S. Hou, J.F. Lee, T.C. Lai, C.C. Liu, C.L. Liu, T.F. Tseng, C.S. Tsai, T.C. Shin, Preseismic deformation and co-seismic displacements associated with the 1999 Chi-Chi, Taiwan earthquake, *Bull. Seismol. Soc. Am.* 91 (2001) 995–1012.
- [17] Y. Okada, Surface deformation due to shear and tensile faults in a half-space, *Bull. Seismol. Soc. Am.* 83 (1985) 1135–1154.
- [18] S.H. Hartzell, T.H. Heaton, Inversion of strong ground motion and teleseismic waveform data for the fault rupture history of the 1979 Imperial Valley, California earthquake, *Bull. Seismol. Soc. Am.* 73 (1983) 1553–1583.
- [19] K.H. Hudnut, Y. Bock, M. Cline, P. Fang, Y. Feng, J. Freymueller, X. Ge, W.K. Gross, D. Jackson, M. Kim, N.E. King, J. Langbein, S.C. Laesen, M. Lisowski, Z.-K. Shen, J. Svarc, J. Zhang, Co-seismic Displacements of the 1992 Landers Earthquake, *Bull. Seismol. Soc. Am.* 84 (1994) 625–645.
- [20] D.V. Wald, T.H. Heaton, K.W. Hudnut, Slip history of the 1994 Northridge, California, earthquake determined from strong-motion, teleseismic, GPS, and leveling data, *Bull. Seismol. Soc. Am.* 86 (1996) s49–s70.
- [21] C.Y. Wang, C.L. Lee, H.Y. Yen, Mapping the northern portion of the Chelungpu Fault, Taiwan by shallow reflection seismic, *Geophys. Res. Lett.* 29 (2002) 951–954.
- [22] S.J. Lee, K.F. Ma, Rupture process of the 1999 Chi-Chi, Taiwan, earthquake from the inversion of teleseismic data, *TAO* 11 (2000) 591–608.
- [23] L. Knopoff, Energy release in earthquakes, *Geophys. J. R. Astron. Soc.* 1 (1958) 44–52.